energies

MDPI

Article

Modeling and Experimental Investigation of Electromagnetic Interference (EMI) for SiC-Based Motor Drive

Yingzhe Wu [1], Shan Yin [2,*], Hui Li [1] and Minghai Dong [1]

[1] School of Aeronautics and Astronautics, University of Electronic Science and Technology of China, Chengdu 611731, China; microuestc@163.com (Y.W.); kelly.li@126.com (H.L.); minh@std.uestc.edu.cn (M.D.)

[2] Microsystem & Terahertz Research Center, Institute of Electronic Engineering, China Academy of Engineering Physics, Chengdu 610200, China

* Correspondence: yinshan@mtrc.ac.cn

Received: 7 September 2020; Accepted: 28 September 2020; Published: 5 October 2020



Abstract: The motor drive has been widely adopted in modern power applications. With the emergency of the next generation wide bandgap semiconductor device, such as silicon carbide (SiC) MOSFET, performance of the motor drive can be improved in terms of efficiency, power density, and reliability. However, the fast switching transient and serious switching ringing of the SiC MOSFET can cause unwanted high-frequency (HF) electromagnetic interference (EMI), which may significantly reduce the reliability of the motor drive in many aspects. In order to comprehensively reveal the mechanism of the EMI previously used in motor drives using SiC MOSFET, this paper plans to analyze the influences of both HF impedance of the motor and switching characteristics of the SiC MOSFET. A simulation model for motor drives has been proposed, which contains the HF circuit model of the motor as well as a semi-behavioral analytical model of the SiC MOSFET. Since the model shows a good agreement with the experimentally measured results on spectra of drain-source voltage of the SiC MOSFET (v_{ds}), phase to ground voltage of the motor (v_{phase}), CM voltage (v_{cm}), phase current of the motor (i_{dm}), and CM current (i_{cm}), it can be adopted to quantitatively investigate the influence of the motor impedance on EMI through frequency-domain analysis. Additionally, the impacts of switching characteristics of SiC MOSFET on EMI are also well studied according to relative experiment results in terms of switching speed, switching frequency, and switching ringing. Based on the analysis above, the relationship between motor impedance, switching characteristics of the SiC MOSFET, and HF EMI can be figured out, which is able to provide much helpful assistance for application of the motor drive.

Keywords: electromagnetic interference (EMI); motor drive; silicon carbide (SiC) MOSFET; motor impedance; switching characteristics

1. Introduction

The motor drive has been recognized as the heart component in modern power applications, such as electric aircraft, maritime, railway transportation as well as new energy vehicles. With the enhanced demands in efficiency and power density, a more effective power converter is required for the motor drive. However, most power converters adopt traditional silicon (Si) insulated gate bipolar transistors (IGBT) and metal oxide semiconductor field effect transistors (MOSFET), which can not guarantee larger efficiency and higher power density due to the limitation of the Si material [1]. In order to improve efficiency and power density of the motor drive, the next generation semiconductor device, such as silicon carbide (SiC) MOSFET, should be considered for applications [2].

Compared with Si IGBT and MOSFET, SiC MOSFET is mainly characterized by faster switching speed, lower switching loss, and higher available operation temperature, which contribute to its greater

efficiency, higher power density, and improved reliability for motor drives [3–6]. However, the high-frequency (HF) electromagnetic interference (EMI) previously used in the motor drive becomes more serious because of the rapid switching speed and obvious switching ringing caused by SiC MOSFET. Moreover, the SiC MOSFET enables higher switching frequency, which also intensifies the HF EMI dramatically [7,8]. As a consequence, the HF EMI should be paid much more attention when applying motor drives based on SiC MOSFET.

The EMI previously used in motor drives can always be represented by common mode (CM) voltage and CM current. The CM voltage can be considered as the origination of the bearing voltage [9,10]. Once the bearing voltage reaches its threshold value, it can cause electric discharge (ED) current that may damage the motor [10,11]. The CM current can flow into other electric equipment through grounding lines, which may significantly reduce reliability of the whole system. Meanwhile, the HF components of the CM current can reach the bearing through HF parasitic effect, which may induce premature bearing failure. In addition, the impedance mismatches between cable and motor accompanied with rapid switching speed of the SiC MOSFET, serious voltage surge can also be observed on motor terminals, which may lead to severe electric insulation issue of the motor [12,13].

Recently, many researches have been focused on the prediction of bearing voltage, CM voltage, CM current, and overvoltage phenomenon with HF modeling of the motor. Equivalent circuit models for evaluating bearing voltage [10,11], CM voltage [14,15], CM current [14–16], and overvoltage on motor terminals [12,13,15] have been proposed. However, these works have not properly considered the impact of switching behavior of the semiconductor device, which is widely considered as the source of the EMI [17]. For instance, the switching transients of the semiconductor device are approximated as ideal step waveform in [13,15]. Meanwhile, the CM and differential mode (DM) impedances of the motor, especially at middle frequency range (100 kHz∼1 MHz), can not be well represented by these models [10,11,13–16], which is responsible for deviations between calculated and experimental measured results.

In [18], the authors indicated that the level of EMI can be effectively estimated through analyzing the spectrum of switching waveform of the semiconductor device. Based on the statement above, the works in [8,19] have investigated the relationship between switching characteristics of the SiC MOSFET and EMI with spectrum analysis. However, the influence of motor impedance has been neglected in [8,19], which is considered as propagation path of the EMI. A comprehensive modeling of the motor drive has been proposed in [20]. In this work, the HF impedance characteristics of the motor and switching behavior of the semiconductor device are modeled and simulated by SPICE for EMI prediction. However, the HF modeling of the motor is based on curve fitting method, which can not be used to reveal the mechanism of the EMI previously used in motor drives due to the lack of physical meanings. Additionally, the driving strategy of the motor, such as space vector modulation (SVM), can not be realized by SPICE. As a result, the simulation is implemented by switching one of the six semiconductor devices in the converter. Generally, there are few publications that have focused on analysis of both motor impedance and switching characteristics of the SiC MOSFET for EMI investigation in motor drive.

In this paper, we have comprehensively analyzed the EMI previously used in motor drives based on modeling and experimental investigation. Compared with other existing works, the main contributions of this paper can be summarized as:

- A simulation model of the motor drive is proposed, which contains an improved HF circuit model of the motor and simplified behavior model of the SiC MOSFET. Meanwhile, the simulation can be carried out by Simulink, which is able to easily realize the SVM driving strategy of the motor. The simulated results show a good agreement with the measured ones because the modeling of the motor impedance and switching behavior of the SiC MOSFET exhibit sufficient accuracy.

- Influence of motor impedance on EMI can be well demonstrated through frequency-domain analysis based on simulation results including the spectra of drain-source voltage of the SiC MOSFET (v_{ds}), phase to ground voltage of the motor (v_{phase}), CM voltage (v_{cm}), phase current of the motor (i_{dm}), and CM current (i_{cm}). Moreover, impacts of switching characteristics of the SiC MOSFET on EMI are also well investigated with relative experimental results in terms of switching speed, switching frequency, and switching ringing.

The rest of the paper is organized as follows. In Section 2, the characteristics of motor drives, including motor impedance and switching behavior of the SiC MOSFET, have been analyzed. Then, the modeling of the motor drive is elaborated in Section 3, which contains HF modeling of the motor and simplified modeling of the switching behavior of SiC MOSFET. Simulation and experiment results are presented and analyzed in Section 4. Influence of motor impedance on EMI are demonstrated through frequency-domain analysis with simulation in Section 5. Meanwhile, impacts of switching characteristics of the SiC MOSFET on EMI in motor drives are elaborated with relative experiment results in Section 6. Finally, the conclusions are summarized in Section 7.

2. Characteristics of the Motor Drive Based on SiC MOSFET

The scheme of a typical motor drive is shown in Figure 1. The power converter is constituted by three half-bridges, and each half-bridge contains two SiC MOSFETs. The cables are replaced by copper wires (L_c), which connect between motor terminals and output nodes of the converter. Different from the cables, the impedance characteristic of the wire can be considered as inductive in a wide frequency range. The the CM propagation path is formed by connecting motor frame to the neutral point (o) with a grounding line (L_g). Meanwhile, the CM coupling path between MOSFET and heat sink can be removed by using the separated heat sinks [21]. L_{loop} is the lumped stray inductance in the power circuit of the converter, which mainly contributes to the HF ringings on v_{ds} during switching transients. Consequently, based on the above descriptions, the CM equivalent circuit of the motor drive can be obtained (see Figure 2).

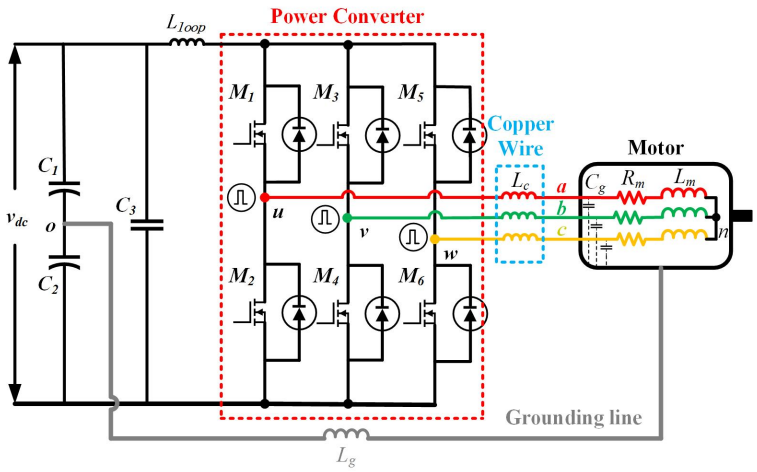

Figure 1. Scheme of a typical motor drive.

According to Figure 2, the CM current can be expressed as:

$$i_{cm} = \frac{v_0}{Z_C + Z_{cm}} \tag{1}$$

where, Z_c means the CM impedance of the dc-link capacitors ($C = C_1 + C_2$), and Z_{cm} represents the CM impedance of the motor plus connection wire and grounding line. The v_0 is the source of CM EMI, and can be written as:

$$v_0 = \frac{1}{3}\left(v_{uo} + v_{vo} + v_{wo}\right) \tag{2}$$

in which, v_{uo}, v_{vo}, v_{wo} represent converter output to ground voltage, which can be viewed as drain-source voltage of the SiC MOSFET because $v_{uo} = v_{ds2} - v_{dc}/2$. The v_{ds2} means the drain-source voltage of the low-side SiC MOSFET of the power converter, such as M_2, illustrated in Figure 1.

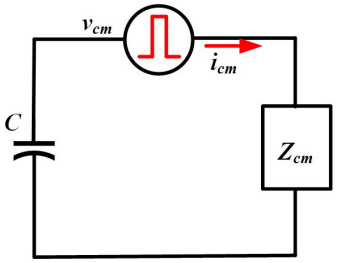

Figure 2. CM equivalent circuit of the motor drive.

Based on (1) and (2), it can be observed that the HF impedance of the motor plus connection wire and grounding line provides propagation path, which impacts the CM current flows through the system. The switching behavior of the SiC MOSFET is the source of EMI, which determines v_{phase} and v_{cm}. In order to comprehensively reveal the mechanism of the EMI in motor drives, influences of motor impedance and switching performance of the SiC MOSFET should be considered together.

2.1. HF Impedance of the Motor

The HF impedance of the motor can be obtained with impedance analyzer. In this study, WK 6500B is adopted to measure the impedance of the motor from 100 Hz to 10 MHz. The measurement of CM and DM impedances of the motor is given in Figure 3. The CM impedance is measured between motor terminals connected together and motor frame, and the DM impedance is measured between the terminal of one phase and the terminals of the other two phases connected together [22]. And the measurement results of CM and DM impedances are shown in Figure 4. Figure 4a illustrates the CM impedance of the motor with and without connection wire and grounding line. With the influence of the wires and parasitic capacitors of the motor (C_g presented in Figure 1), the CM resonance is formed around 4 MHz. Similarly, the DM impedance of the motor (Z_{dm}) with and without connection wire and grounding line is shown in Figure 4b. The DM resonance which appears at approximately 8 MHz is also attributed to the equivalent inductance of the wires (L_s and L_g shown in Figure 1) and C_g. Both CM and DM resonances deserve much more consideration because they have played significant roles in determining v_{phase} and v_{cm}, which closely relate to the level of EMI.

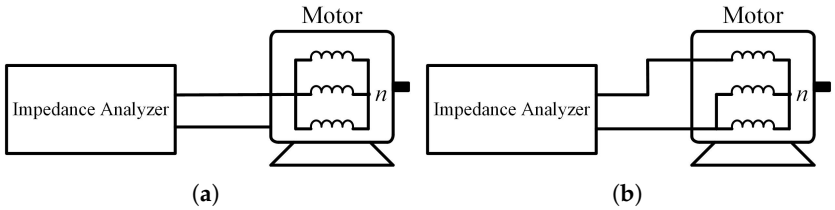

Figure 3. Measurement of the CM and DM impedances of the motor: (**a**) CM impedance, (**b**) DM impedance.

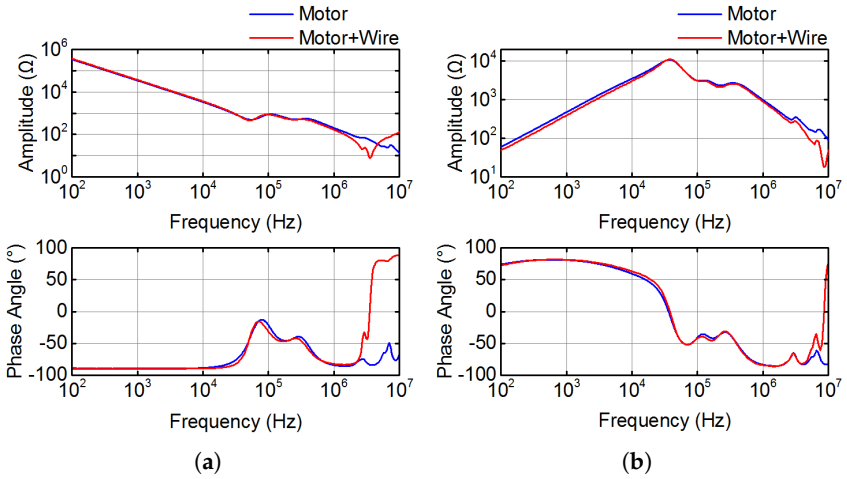

Figure 4. The CM and DM impedances of the motor: (**a**) CM impedance, (**b**) DM impedance.

2.2. Switching Behavior of the SiC MOSFET

Generally, the analytical switching waveform of the drain-source voltage of the SiC MOSFET can be approximated as asymmetric trapezoid wave plus decayed sine wave (see Figure 5). With the Fourier Transformation, the spectrum of v_{ds} can be derived in (3)∼(5) [23].

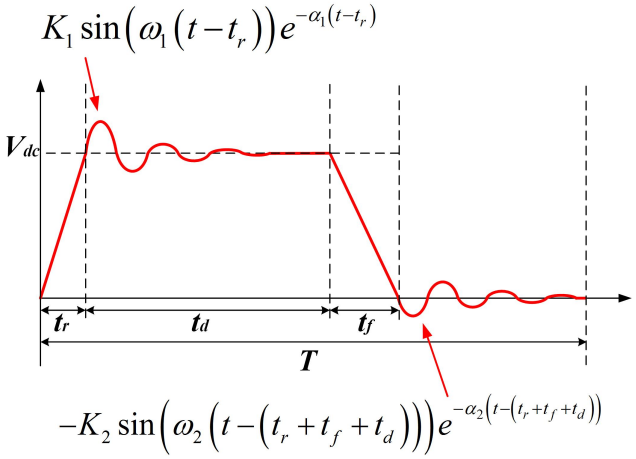

Figure 5. Analytical switching waveform of the drain-source voltage of the SiC MOSFET.

$$
\begin{aligned}
a_n = & \underbrace{\frac{V_{dc}T}{4n^2\pi^2}\begin{pmatrix} \frac{1}{t_f}\left(1-e^{-jn\frac{2\pi}{T}t_f}\right)e^{-jn\frac{2\pi}{T}(t_t+t_d)} \\ -\frac{1}{t_r}\left(1-e^{-jn\frac{2\pi}{T}t_r}\right) \end{pmatrix}}_{Asymmetrical-trapezoidal-waveform} \\
& + \underbrace{\frac{K_1\omega_1}{T\left(C_1^2+{\omega_1}^2\right)}e^{-jn\frac{2\pi}{T}t_r}\begin{pmatrix} 1-\cos\left(\omega_1 t_d\right)e^{-C_1 t_d} \\ -\frac{C_1\sin(\omega_1 t_d)}{\omega_1}e^{-C_1 t_d} \end{pmatrix}}_{Turn-off-oscillation} \\
& - \underbrace{\frac{K_2\omega_2}{T\left(C_2^2+{\omega_2}^2\right)}e^{-jn\frac{2\pi}{T}t_0}\begin{pmatrix} 1-\cos\left(\omega_2\left(T-t_0\right)\right)e^{-C_2(T-t_0)} \\ -\frac{C_2\sin(\omega_2(T-t_0))}{\omega_2}e^{-C_2(T-t_0)} \end{pmatrix}}_{Turn-on-oscillation}
\end{aligned}
\tag{3}
$$

$$\begin{cases} C_1 = \alpha_1 + jn\frac{2\pi}{T} \\ C_2 = \alpha_2 + jn\frac{2\pi}{T} \\ t_0 = t_r + t_f + t_d \end{cases}. \quad (4)$$

$$S(n) = |2a_n\delta(f - nf_0)|, (f_0 = 1/T). \quad (5)$$

According to (3)∼(5), it can be figured out that the voltage commutation transient (including duration of t_r and t_f) interprets attenuation rate of the spectrum [8], and the switching ringings are responsible for the spikes at HF range (tens of mega hearts) [23]. Additionally, the switching frequency is closely related to the amplitude of the spectrum, and can be considered as another critical factor that significantly impacts the EMI in motor drives.

3. Modeling of the SiC-Based Motor Drive

3.1. HF Modeling of the Motor

The impedance characteristics of the motor can be depicted through HF modeling. In this case, based on impedance curves and wingding configurations of the motor, an equivalent circuit (see Figure 6) is proposed to illustrate the impedance characteristics of the motor.

According to Figure 6, the winding of the motor is mainly composed by three parts. The part I winding is mainly responsible for describing CM impedance at the whole frequency range (100 Hz∼ 10 MHz), while it also impacts DM impedance in the middle frequency range (0.01∼1 MHz). The part II winding mainly determines the DM impedance at low frequency range (100 Hz∼10 kHz), and the part III winding impacts the DM impedance from 10 kHz∼1 MHz. The series L_{j1i}-R_{j1i}-C_{j1i} ($i = 1, 2$) and L_{j2}-R_{j2}-C_{j2} branches reflect interturn effects of the Part I and II windings, respectively. The series L_T-R_T-C_T branch represents the leakage effect occurs on first few turns of the part I winding, which largely impacts both CM and DM impedance at the middle frequency range. The C_{gi} (i = 1, 2, 3, 4) are parasitic capacitances between winding and frame of the motor, and the R_g can be considered as the terminal resistance of the motor. Additionally, the EMF block reflects the generated electromotive force when motor is operating.

The values of the electric parameters described above can be determined (see Table 1) based on the method elaborated in our previous works [22]. Figure 7 compares the calculated and measured impedance of the motor. The calculated CM and DM impedances of the motor are in nice accordance with the ones measured by impedance analyzer. It is obvious that the proposed HF model can describe impedance of the motor with sufficient accuracy, especially in the middle frequency range (100 kHz∼1 MHz), compared with the ones in [10,11,13–16].

Table 1. Values of electric parameters of the model.

Parameter	Value	Parameter	Value	Parameter	Value
C_{g1}	0.25 nF	R_{22}	189 Ω	L_{11}	9 mH
C_{g2}	0.98 nF	R_{23}	350 Ω	L_{21}	9.6 mH
C_{g3}	30 pF	R_{24}	630 Ω	L_{22}	5.3 mH
C_{g4}	30 pF	R_{25}	1.12 kΩ	L_{23}	4.9 mH
C_{j11}	14.4 pF	R_{31}	100 kΩ	L_{24}	4.2 mH
C_{j12}	37.4 pF	R_g	4.2 Ω	L_{25}	4.0 mH
C_{j2}	1.86 nF	R_{j11}	650 Ω	L_{j11}	0.21 mH
C_T	0.19 nF	R_{j12}	260 Ω	L_{j12}	17.4 μH
R_{11}	5.3 kΩ	R_{j2}	9.47 kΩ	L_{j2}	6.9 mH
R_{21}	120 Ω	R_T	3.23 kΩ	L_T	1.9 mH

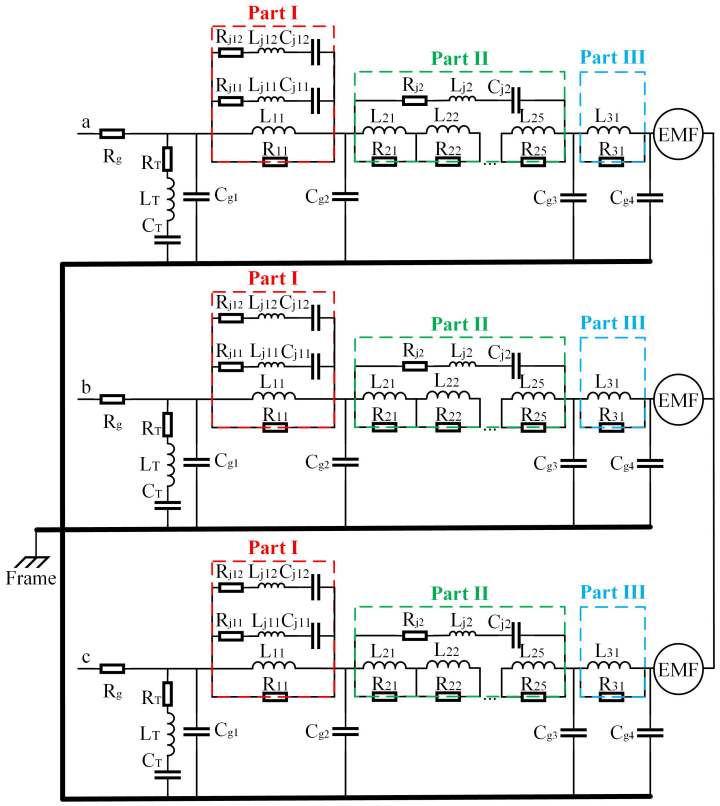

Figure 6. HF circuit model of the three-phase motor with star connection.

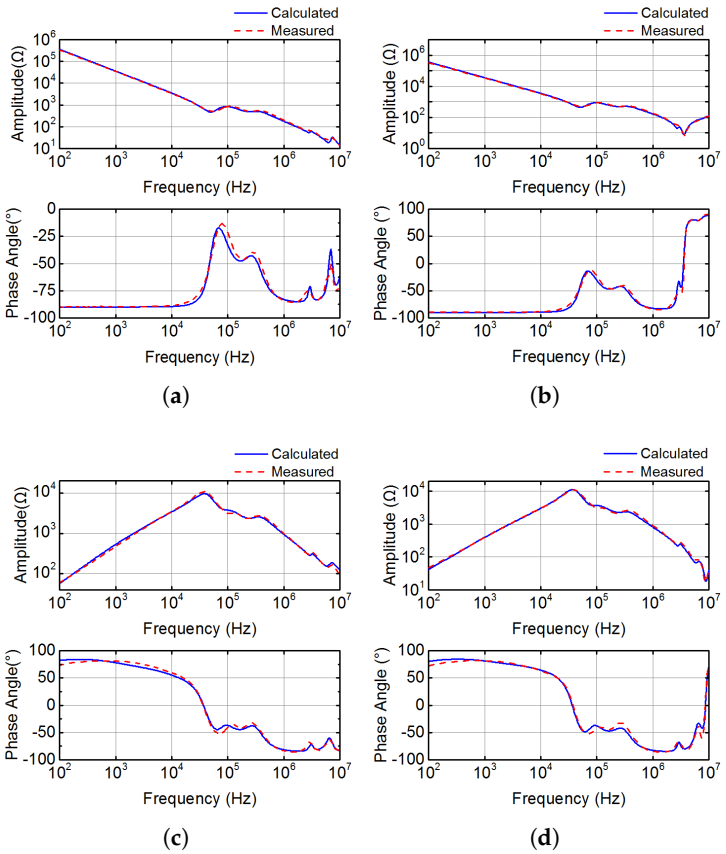

Figure 7. Comparisons between calculated and measured impedances of the motor: (**a**) CM impedance without wire, (**b**) CM impedance with wire, (**c**) DM impedance without wire, (**d**) DM impedance with wire.

3.2. Simplified Modeling of the SiC MOSFET

According to operation mechanism of the SiC MOSFET, the voltage commutation is mainly determined by gate resistance, drain and source inductances, and junction capacitances (C_{gs}, C_{gd}, and C_{ds}) [24,25]. The switching ringing can be attributed to the resonance between output capacitance ($C_{oss} = C_{gd} + C_{ds}$) and summation of stray inductance in the circuit [23]. Analytical modeling presented in [23–25] can accurately illustrate the switching behavior of the SiC MOSFET. In general, these models are suitable for several micro-seconds level system simulation.

Since the operation frequency of motor is no more than several tens hertz, the simulation time for motor drives should be no less than several hundreds milliseconds, which makes the aforementioned analytical models time consuming, and not suitable for system simulation of the motor drive. As a result, simplified modeling should be proposed to improve the calculation efficiency.

The voltage rise and fall stages during switching transient are linearized for simplification in this case. Therefore, the voltage commutation can be realized by a controlled voltage source. Meanwhile, the second order $L - R - C$ circuit is adopted to represent the switching ringing on v_{ds}. The simplified behavior model of the SiC MOSFET is shown in Figure 8. Since most of physical mechanisms during switching transient are ignored, the calculation speed of the model can be enhanced significantly. However, the accuracy of the model will be reduced. Obviously, the trade-off between calculation speed and accuracy of the model should be well balanced.

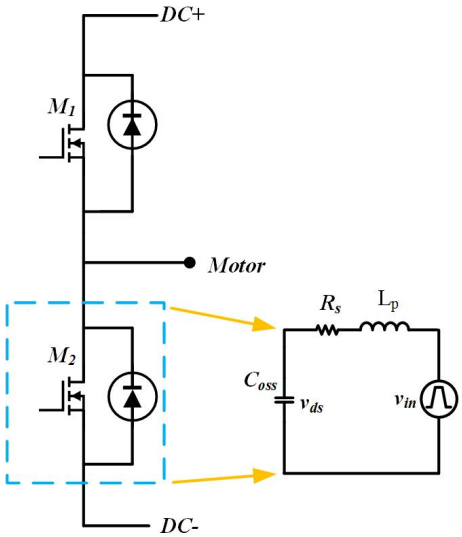

Figure 8. Simplified modeling of switching behavior of SiC MOSFET.

Figure 9 illustrates the comparisons between calculated and measured waveforms of v_{ds} during switching transient of the SiC MOSFET. According to operation principles of the SiC MOSFET, the slew rate of v_{ds} is determined by $L_p \cdot \frac{di_d}{dt}$ during current commutation, and the charging and discharging rate of the gate-drain capacitance C_{gd} is attributed to slew rate of v_{ds} during voltage commutation. Since the dv_{ds}/dt is approximated as a constant value, the voltage rise and fall stages can not be accurately illustrated in the modeling. However, based on statement in [8], the spectrum envelop is mainly determined by rise and fall time (t_r and t_f) of the v_{ds}, which indicates that the model can correctly reflect the spectrum of v_{ds} because the calculated t_r and t_f are the same with the measured ones.

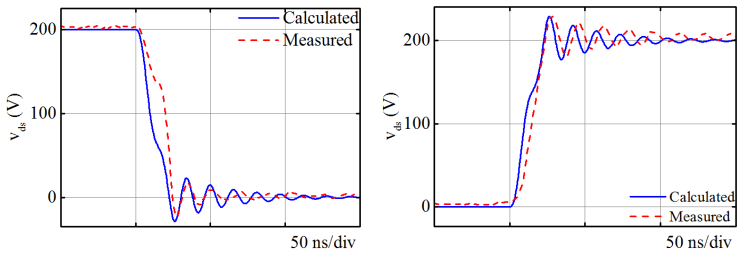

Figure 9. Calculated and measured waveforms of v_{ds} during switching transient: (**a**) turn-on, (**b**) turn-off.

4. Simulation and Experiment Results

The simulation model of the motor drive is realized by Simulink (see Figure 10), which contains simplified model of switching action for SiC MOSFET, and HF model of the motor, connection wire, ground line. Furthermore, the SVM algorithm is also implemented with Simulink. The waveforms of v_{ds}, v_{phase}, v_{cm}, i_{dm}, and i_{cm} are obtained in the simulation.

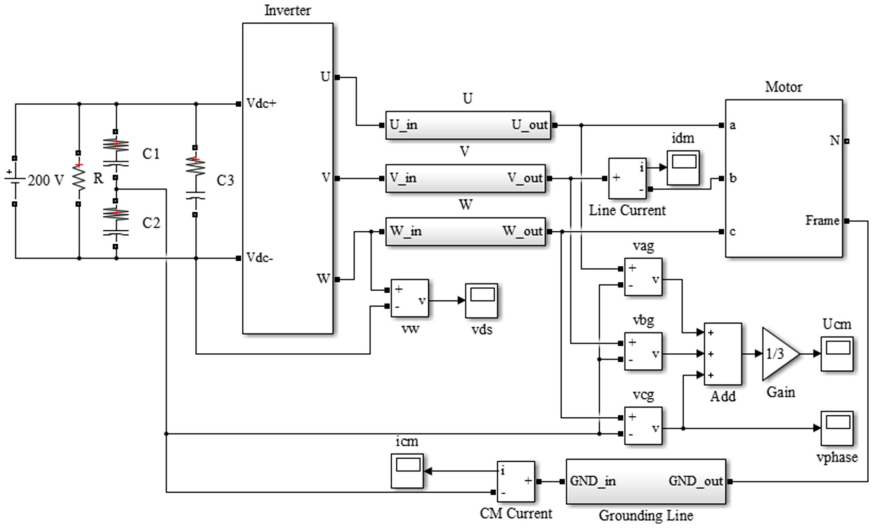

Figure 10. Simulation model of the motor drive.

A three-phase permanent magnet synchronous motor (see Figure 11a) is selected in this study. The detailed parameters of the motor are listed in Table 2. The main circuit board of the motor drive is shown in Figure 11b, which contains three phase-legs. Each phase-leg is constituted by two SiC MOSFETs (C2M0080120D from Wolfspeed). Six isolated gate drivers, designed with ACPL-W346 from Avago, are used to drive the SiC MOSFETs, and three groups of dc-link capacitors are adopted to limit dc-bus voltage variation. The output nodes of the inverter (u, v, and w) are connected to the motor terminals (a, b, and c) with copper wires, and the motor frame is connected to the neutral point o with grounding line. Six separated heat-sinks are attached on the top of the MOSFETs. HF parasitic effect between MOSFET and heat-sink can be neglected once the heat sink is floating in the system. STM32F103 is adopted as the core of the control unit, which is responsible for driving the motor with SVM algorithm. The dc power supply is 200 V in the experiment. The switching frequency of the power inverter is set as 80 kHz, and the motor is operating at 600 rpm. The voltage and current waveforms of the motor drive are obtained with Lecroy's Wave-Runner 8404-M. Three high-voltage and high-bandwidth differential probes HVD3106 (1.5 kV, 120 MHz) are utilized to measure the phase to ground voltage including v_{ao}, v_{bo}, and v_{co}. The CM and line current of the motor are measured with a high-bandwidth current probe TCP312A (30 A, 100 MHz).

Table 2. Parameters of the motor in the test.

Parameters	Values
Rated Power	3 kW
Rated Voltage	380 V
Maximum current	6.2 A
Pole Pairs	2
Rotor Configuration	Surface Mounted
Winding Connection	Star

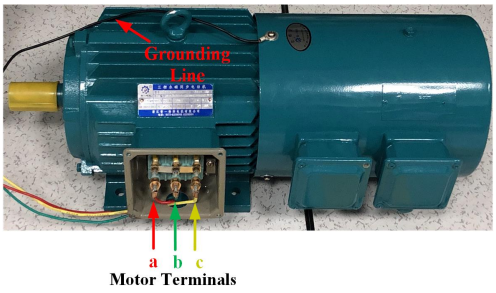

(**a**)

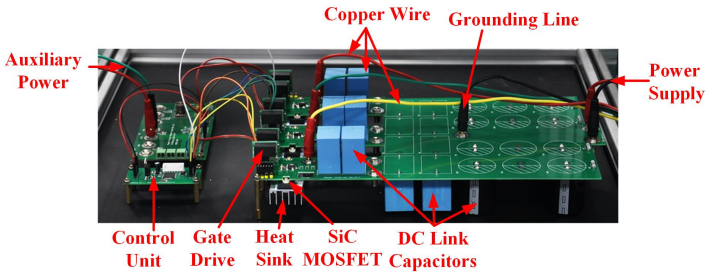

(**b**)

Figure 11. Experiment bench of the motor drive: (**a**) Motor, (**b**) Main circuit board of the motor drive.

4.1. Calculated and Measured Spectra of v_{ds}, v_{phase}, and v_{cm}

Figure 12a illustrates the calculated and measured spectra of v_{ds}. Since the calculated waveform of v_{ds} is in nice accordance with the measured ones (see Figure 5), the calculated spectra of v_{ds} can also fit well with the measured ones.

Figure 12b shows the comparison between calculated and measured spectra of v_{phase}. It can be observed that the measured spectrum of v_{phase} is less than that of the calculated ones from 5 to 10 MHz. This is mainly due to the ignorance of contact impedances of the connectors between inverter output nodes and copper wires in the model. Such contact impedance can induce some voltage drops at this frequency range (5∼10 MHz) in the measurement.

Figure 12c depicts the calculated and measured spectra of v_{cm}. The calculated spectrum of v_{cm} is in nice accordance with the measured ones below 5 MHz. However, the calculated and measured results cannot fit well with each other from 5 to 30 MHz. Unlike the measured spectrum of v_{cm}, the spike cannot be observed on the calculated result around 8 MHz.

We should notice that v_{cm} is synthesized by v_{phase}, and can be expressed as the following equation.

$$v_{cm} = \frac{1}{3}\left(v_{ao} + v_{bo} + v_{co}\right). \tag{6}$$

Therefore, influence of the contact impedance on v_{phase} (v_{ao}, v_{bo}, and v_{co}) mentioned above is responsible for such deviations. It should also be found that unlike simulation, propagation delay

indeed exists in each voltage probe, which can cause asymmetric phase angle between the measured v_{ao}, v_{bo}, and v_{co} during experiment. As a consequence, the voltage components around 8 MHz can not be canceled completely during synthesizing.

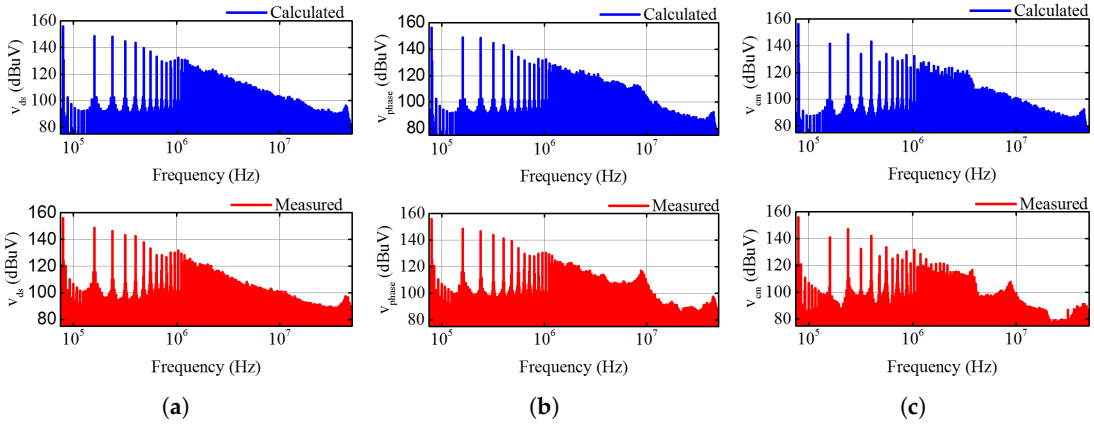

Figure 12. Calculated and measured spectra of v_{ds}, v_{phase} and v_{cm}: (**a**) v_{ds}, (**b**) v_{phase}, (**c**) v_{cm}.

4.2. Calculated and Measured Spectra of i_{dm} and i_{cm}

Figure 13 shows the calculated and measured spectra of i_{dm} and i_{cm}. The calculated i_{dm} and i_{cm} are fitted well with the measured ones, and the spectra peaks around 4 and 8 MHz can also be well reflected by the model. Therefore, it can be confirmed that the model can effectively predict the line current and CM current in motor drives.

In addition, it can be observed that v_{phase}, v_{cm}, and impedance of the motor are responsible for i_{dm} and i_{cm} according to (7). In other words, the accuracy of the calculated v_{phase} and v_{cm} can also be verified due to the nice accordance in the calculated and measured amplitude of i_{dm}, i_{cm} and motor impedance (including Z_{dm} and Z_{cm}).

$$\begin{cases} i_{dm} = v_{phase} / Z_{dm} \\ i_{cm} = v_{cm} / Z_{cm} \end{cases} . \tag{7}$$

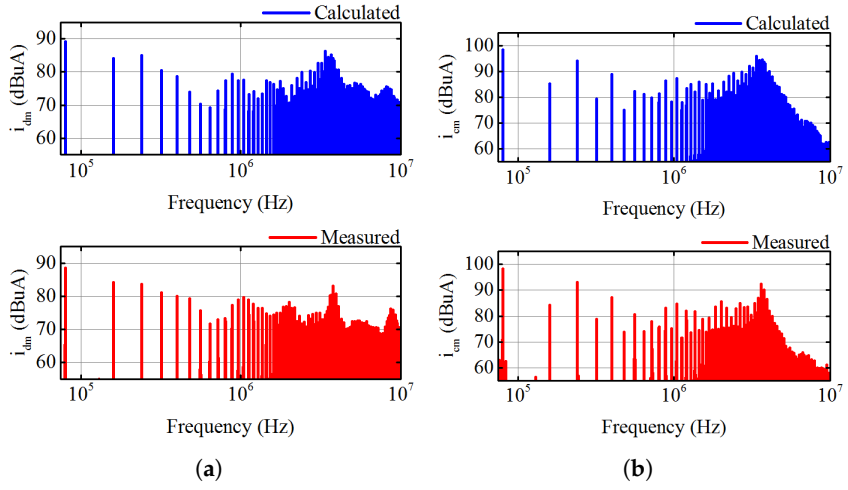

Figure 13. Calculated and measured spectra of i_{dm} and i_{cm}: (**a**) i_{dm}, (**b**) i_{cm}.

5. Impacts of the Impedance Characteristics on EMI in Motor Drive

Since the effectiveness of the proposed model has been verified, we plan to analysis the relations between v_{ds}, v_{phase}, v_{cm}, i_{dm}, i_{cm} as well as motor impedance to demonstrate impacts of impedance characteristics on EMI in motor drives with the model in this section.

5.1. Comparison between v_{ds} and v_{phase}

In order to elaborate the relationship between v_{ds} and v_{phase}, the following assumptions should be made at first.

- M_1 is turning on, M_2 is turning off, M_3 and M_5 are turned off, M_4 and M_6 are turned on (see Figure 1).
- The voltage drops on SiC MOSFETs and its body diodes are neglected in this condition.

Therefore, the DM propagation path of the HF components can be plotted (see Figure 14). The motor winding can be considered as open circuit in this case because the HF components (above 1 MHz) can not penetrate the winding deeply [26,27]. Then, the DM equivalent circuit of the motor drive can be obtained accordingly (see Figure 15).

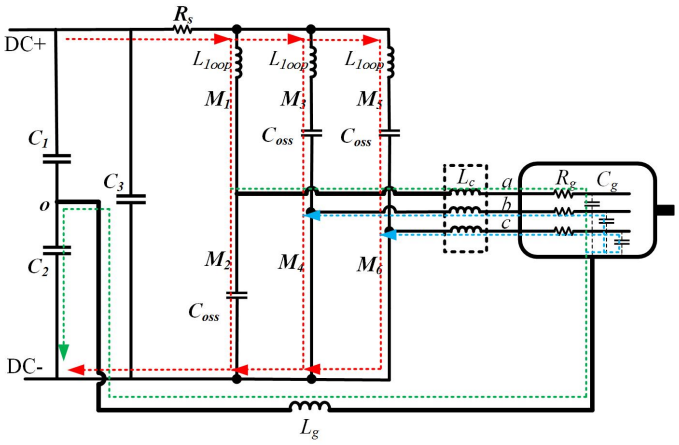

Figure 14. DM propagation path of the HF components in motor drives.

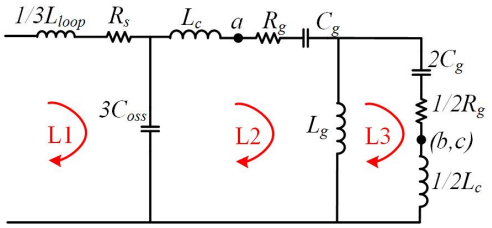

Figure 15. DM equivalent circuit of the motor drive in HF range.

Three $L-R-C$ resonance loops (L_1, L_2, and L_3) can be observed in Figure 15, which mainly contribute to resonances shown in Figure 16. It can be observed that the LF resonances (less than 10 MHz) attribute to interactions between copper wire (L_c), grounding line (L_g), and parasitic capacitance of the motor (C_{g1}), and the HF resonance (around 45 MHz) owes to stray inductance in power circuit (L_{loop}) and output capacitance of the SiC MOSFET (C_{oss}).

Figure 17 illustrates the calculated time-domain waveforms and spectra of v_{ds} and v_{phase}. It is obvious that the additional ringings and spikes on v_{phase} are attributed to LF resonances described above. It can be also observed that the increased impedances of L_c and L_g cause non-negligible voltage drops, which contribute to the slower slew rate and reduced amplitude in time- and frequency-domain waveforms of v_{phase} at a higher frequency range (above 10 MHz).

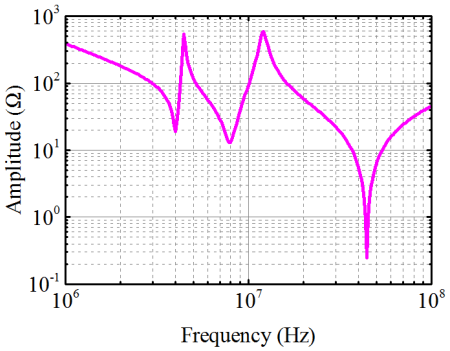

Figure 16. Frequency-domain characteristics of the DM circuit in HF range.

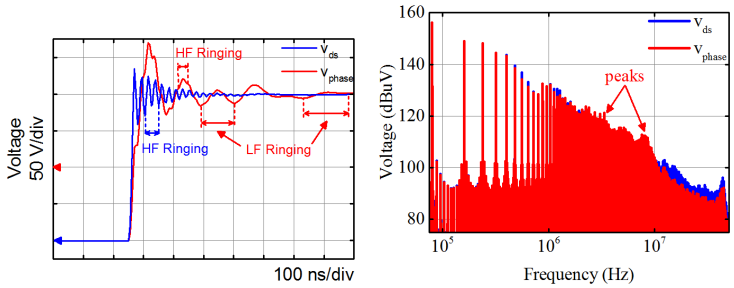

(**a**) (**b**)

Figure 17. Comparison between calculated v_{ds} and v_{phase}: (**a**) Time-domain waveforms, (**b**) Spectra.

5.2. Comparison between v_{ds} and v_{cm}

In order to elaborate the relationship between v_{ds} and v_{cm}, the following assumptions should be made initially.

- M_1 is turning off, M_2 is turning on, M_3 and M_5 are turned off, M_4 and M_6 are turned on (see Figure 1).
- The voltage drops on SiC MOSFETs and its body diodes are neglected in this condition.

Therefore, the CM propagation path of the HF components can be plotted (see Figure 18). Similarly, the CM equivalent circuit of the motor drive can be obtained accordingly (see Figure 19).

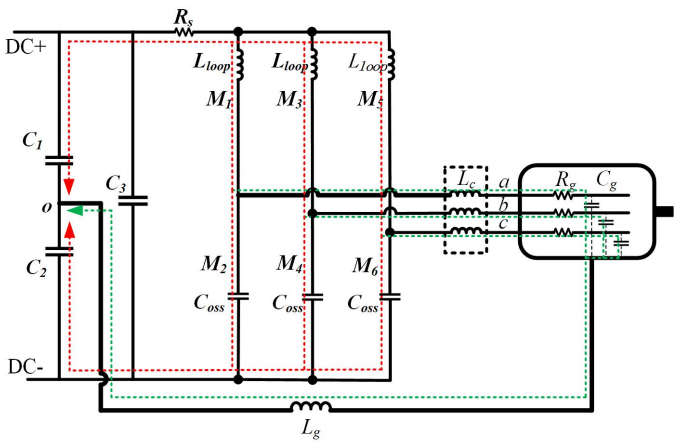

Figure 18. CM propagation path of the HF components in motor drives.

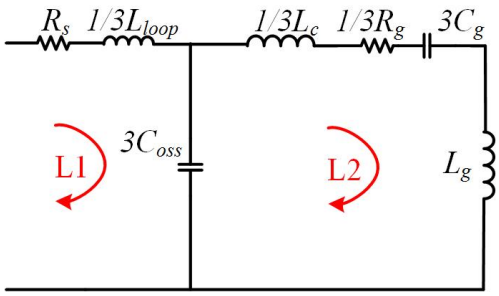

Figure 19. CM equivalent circuit of the motor drive in HF range.

Two $L-R-C$ resonance loops (L_1 and L_2) can be observed in Figure 19, which lead to resonances shown in Figure 20. It can be observed that the LF resonance (around 4 MHz) owes to impacts of copper wire (L_c), grounding line (L_g), and parasitic capacitance of the motor (C_{g1}), and the HF ones (around 45 MHz) is attributed to stray inductance in power circuit (L_{loop}) and output capacitance of the SiC MOSFET (C_{oss}).

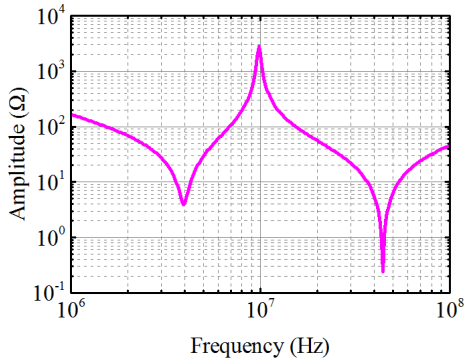

Figure 20. Frequency-domain characteristics of the CM circuit in HF range.

Figure 21 compares the calculated spectra of v_{ds} and v_{cm}. The added peak component on spectrum of v_{cm} can be attributed to the resonance around 4 MHz. From 5 to 10 MHz, the spectrum of v_{cm} drops because harmonics in this frequency range can be canceled during synthesizing process described in (6). The amplitude of v_{cm} spectrum is also less than that of v_{ds} at higher frequency range (above 10 MHz) due to the voltage drops between inverter output nodes and motor terminals.

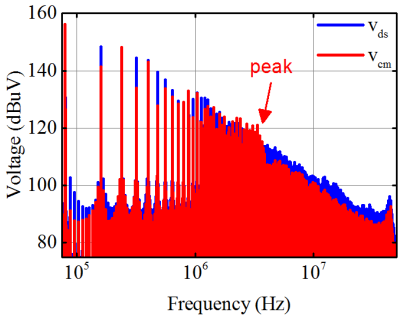

Figure 21. Comparison between calculated spectra of v_{ds} and v_{cm}.

5.3. Comparison between v_{phase} and v_{cm}

Figure 22 depicts the calculated waveforms of v_{phase} and v_{cm} in the time- and frequency-domain. It can be clearly observed that the ringing and spike around 8 MHz on v_{cm} have been removed. According Figures 16 and 20, only two resonances can be observed on frequency-domain characteristics of the CM circuit because the L_3 loop previously used in the DM circuit is bypassed during CM analysis.

It can be also considered that the 8 MHz ringing on v_{cm} can be canceled during synthesizing process depicted in (6).

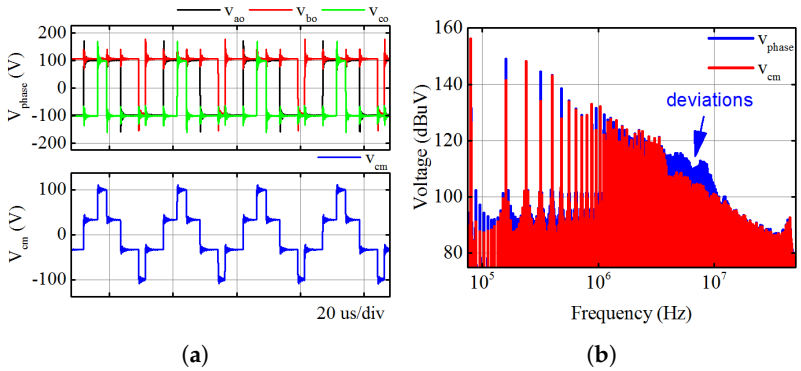

Figure 22. Comparison between calculated v_{phase} and v_{cm}: (**a**) Time-domain waveforms, (**b**) Spectra.

5.4. Comparison between i_{dm} and i_{cm}

Figure 23 shows the calculated spectra of i_{dm} and i_{cm}. At lower frequency range (100 kHz∼5 MHz), CM impedance of the motor is far less than that of DM impedance (see Figure 24). Since the spectrum amplitude of v_{cm} is nearly the same with that of v_{phase} (see Figure 22b), the spectrum amplitude of i_{cm} is larger than that of i_{dm} in this frequency range. The peak component of v_{cm} (≃4 MHz) and lower CM impedance contribute to the spectrum spike of i_{cm} (≃4 MHz). The current spike on spectrum of i_{dm} is much lower due to the larger DM impedance. According to Figure 24, Z_{dm} is almost 5–6 times Z_{cm} from 100 to 5 MHz.

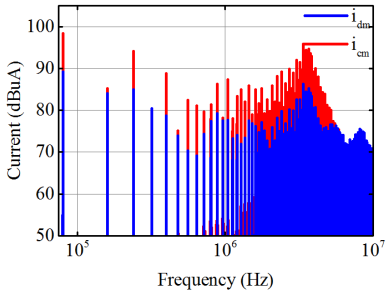

Figure 23. Comparison between calculated spectra of i_{dm} and i_{cm}.

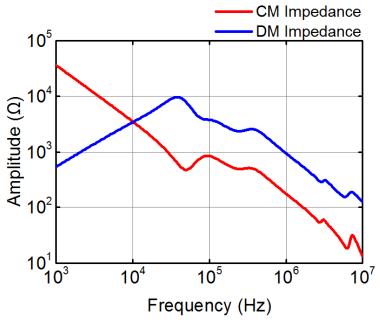

Figure 24. Comparison between calculated CM and DM impedances of the motor.

At higher frequency range (above 5 MHz), the spectrum of v_{cm} drops dramatically, and the deviation between spectrum amplitude of v_{cm} and v_{phase} is about 10 dBuV (see Figure 22b). Accordingly, the spectrum amplitude of i_{cm} attenuates faster. The peak component of i_{dm} (≃ 8 MHz) can be clearly observed due to the spectrum spike on v_{phase}. Although Z_{cm} is still lower than Z_{dm}, there is no spectrum spike on i_{cm} because spectrum amplitude of v_{cm} around 8 MHz is much lower than that of v_{phase}.

5.5. Influence of the Motor Impedance on EMI

Influence of the motor impedance on EMI has been summarized in Figure 25. The switching behavior of the SiC MOSFET is considered as the source of EMI. With the resonances between copper wires, grounding line and parasitic capacitors, the HF harmonics of v_{ds} have been changed, which contributes to the formation of v_{phase} and v_{cm}. Then, with the influence of motor impedance, i_{phase} and i_{cm} can be determined accordingly. Thus, it can be confirmed that the resonances caused by copper wires, grounding line and parasitic capacitors as well as motor impedance significantly impact the level of EMI below 10 MHz. It is obvious that the LF (less than 10 MHz) EMI is expected to be reduced with an added filter, which can modify impedance characteristics of the resonances between L_c, L_g and C_g. In some cases, integrated motor drives have been adopted to minimize the level of EMI, which can improve impedance of the motor drive around resonance frequency [3].

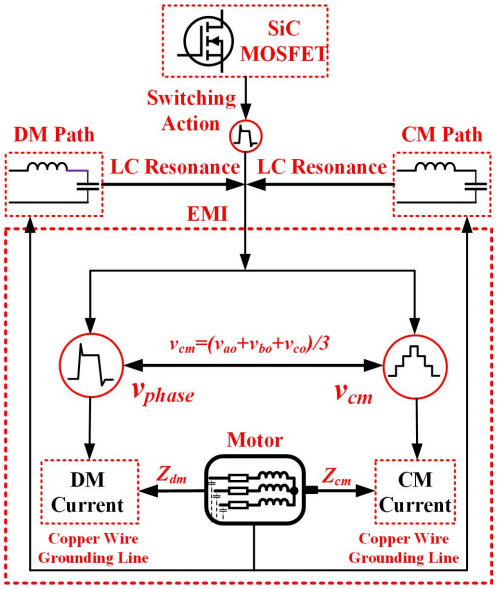

Figure 25. Summarization of the relationship between motor impedance and EMI in motor drives.

6. Impact of the Switching Characteristics of the SiC MOSFET on EMI in Motor Drive

In this section, v_{cm} and i_{cm} are selected as investigation objective to analyze impact of switching characteristics of the SiC MOSFET, including switching speed, switching frequency (f_s), and switching ringing, on EMI in motor drives. Relative experiment results are given in Figures 26 and 27.

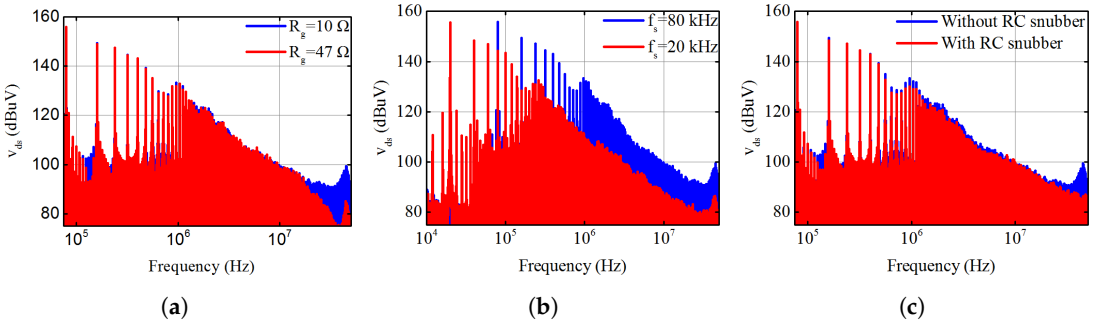

Figure 26. Spectra of the drain-source voltage of the SiC MOSFET: (**a**) $R_{g(ex)}$ = 10 and 47 Ω, (**b**) f_s = 80 and 20 kHz, (**c**) with and without RC snubber.

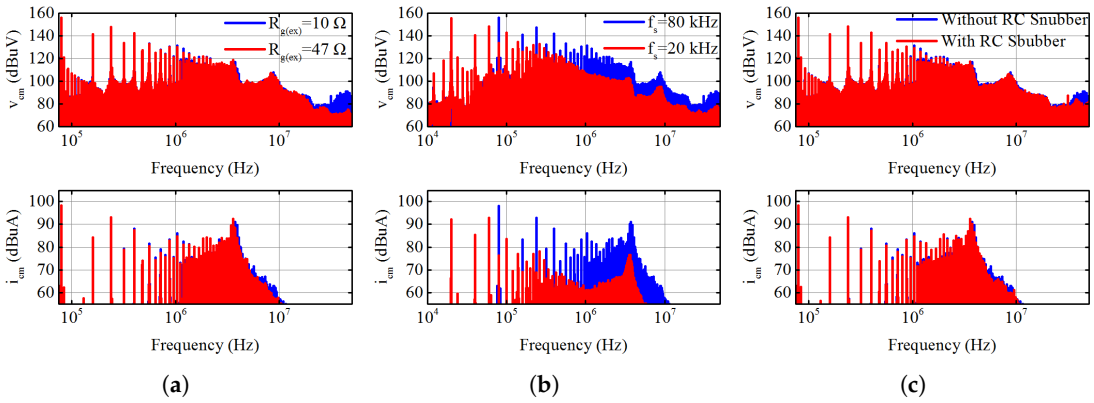

Figure 27. Spectra of CM voltage and CM current: (**a**) $R_{g(ex)}$ = 10 and 47 Ω, (**b**) f_s = 80 and 20 kHz, (**c**) with and without RC snubber.

6.1. Impact of Switching Speed

Variation of parasitic capacitances and inductances can impact switching characteristics of the SiC MOSFET significantly [24]. However, these parasitic parameters must be maintained in small values to guarantee sufficient reliability of the SiC MOSFETs in practical applications. Therefore, regulating the gate resistor ($R_{g(ex)}$) can be considered as an effective method to flexibly change the switching characteristics of the SiC MOSFET. Figure 26a compares the spectra of v_{ds} when $R_{g(ex)}$ equals to 10 and 47 Ω. In this study, the motor speed is 600 rpm, power supply voltage v_{dc} = 200 V, switching frequency f_s = 80 kHz, and gate resistance $R_{g(ex)}$ = 10 and 47 Ω. The amplitude at HF range (above 20 MHz) is reduced with the increased R_g. Additionally, the spectrum spike around 45 MHz is also attenuated once $R_{g(ex)}$ is selected as 47 Ω due to the enlarged damping ratio of the second $L-R-C$ circuit. As a result, the spectrum amplitude of v_{phase} become lower at the frequency range above 20 MHz, and the HF spectrum spikes on v_{cm} around 45 MHz is also reduced when $R_{g(ex)}$ equals to 47 Ω (see Figure 27b). But the i_{cm} is nearly not affected by the variation of the $R_{g(ex)}$.

The spectrum envelop of the drain-source voltage of the SiC MOSFET (v_{ds}) mentioned in [8] is shown in Figure 28. Obviously, the spectrum envelop of the v_{ds} is determined by corner frequencies (f_{c1}, f_{c2}, and f_{c3}), which depends largely on switching characteristics of the SiC MOSFET. Relationships between switching characteristics of the MOSFET and corner frequencies of the spectrum envelop can be expressed as [8]:

$$\begin{cases} f_{c1} = \frac{1}{\pi \min(t_r, t_f)} \\ f_{c2} = \frac{1}{\pi \max(t_r, t_f)} \\ f_{c3} = \frac{2f_s}{\left| e^{-j\pi\left(2t_d + t_r - t_f\right)/T_s} - 1 \right|} \end{cases} \tag{8}$$

in which, t_r, t_f, t_d are rise-time, fall-time and off-time of the SiC MOSFET. f_s is the switching frequency of the SiC MOSFET, and T_s=1/f_s.

We should admit that the switching response speed can be reduced with the increased $R_{g(ex)}$ as well as the corner frequencies (f_{c1} and f_{c2}), but the values of f_{c1} and f_{c2} are still above 10 MHz when R_g increased to 47 Ω. As a result, the LF spectra of v_{cm} and i_{cm} are nearly not affected by the increase of $R_{g(ex)}$ in this case. With continuous increase of the $R_{g(ex)}$, the f_{c1} and f_{c2} will decrease below 10 MHz, and the amplitude of v_{cm} and i_{cm} spectra at the lower frequency range (below 10 MHz) would be weaken. However, the switching loss will be increased dramatically, which may adversely affect efficiency of the motor drive. This view point has been emphasized in [28]. Moreover, slower response speed causes larger preset dead-time zone, which may largely reduce the accuracy of control algorithm.

Consequently, to regulate the gate resistor in a reasonable range can alleviate the HF EMI (above 20 MHz) with slightly increased switching loss, and ensure the accuracy of control algorithm. But for LF EMI (below 10 MHz) mitigation, this method seems less effective.

6.2. Impact of Switching Frequency

Switching frequency of the SiC MOSFET can impact the spectrum of v_{ds} in the whole frequency range. According to (3), the lower switching frequency means the reduced spectrum amplitude of v_{ds}. This view point has also been confirmed in [8]. In this study, the motor speed is 600 rpm, power supply voltage v_{dc} = 200 V, gate resistance $R_{g(ex)}$ = 10 Ω, and switching frequency f_s = 20 and 80 kHz.

Figure 26b compares the spectra of v_{ds} with different switching frequencies (f_s = 20 and 80 kHz). It can be observed that the spectrum amplitude is largely reduced with the lower switching frequency. As a result, the spectra amplitude of v_{cm} and i_{cm} are reduced remarkably when f_s is set as 20 kHz (see Figure 27b). According to Figure 28 and (8), it can be clearly figured out that corner frequency (f_{c3}) will be reduced with lower switching frequency as well as spectrum envelop. The average deviations between thees two cases are more than 10 dBuV. Obviously, the EMI previously used in motor drives can be effectively suppressed with lower switching frequency. However, lower switching frequency can not ensure higher power density, and also reduces controllability as well as robustness of the motor drive. As a result, to make the trade-off between EMI, power density, controllability, and robustness of the motor drive, optimized switching frequency of the SiC MOSFET is recommended.

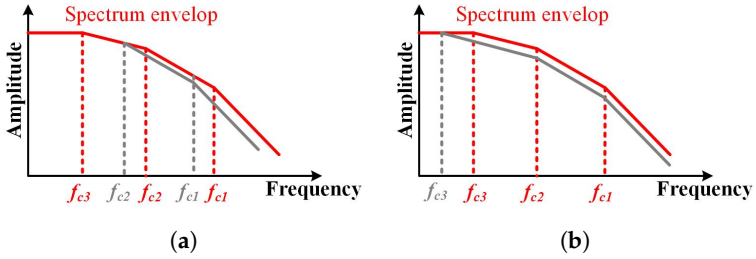

Figure 28. Influence of switching characteristics of SiC MOSFET on spectrum envelop of the drain-source voltage v_{ds}, (**a**) variation of $R_{g(ex)}$, (**b**) variation of f_s.

6.3. Impact of Switching Ringing

Adding RC snubber can effectively suppress the switching ringing on v_{ds}. Therefore, the spikes on spectrum of v_{ds} at a higher frequency range (above 30 MHz in this case) would be mitigated based on (3). In this study, the motor speed is 600 rpm, power supply voltage v_{dc} = 200 V, gate resistance $R_{g(ex)}$ = 10 Ω, switching frequency f_s = 80 kHz, snubber capacitor C_s = 10 nF, and snubber resistor R_s = 10 Ω.

Figure 26c compares the spectrum of v_{ds} with and without RC snubber. It is obvious that the added RC snubber can effectively mitigate the HF switching ringing, and alleviate the amplitude of the spectrum at HF range (above 30 MHz). As a result, the spectrum peak around 45 MHz on v_{cm} is disappeared with the added RC snubber (see Figure 27c).

It should be noticed that the RC snubber is designed to suppress the HF ringing caused by resonance between L_{loop} and C_{oss}, it has limited effect on LF ringing suppression caused by resonance between L_c, L_g, and C_{g1}. The RC snubber can not change the switching speed of the SiC MOSFET [23], as a result, the corner frequencies (f_{c1} and f_{c2}) of the spectrum envelop are also unchanged with the added RC snubber. Therefore, the amplitude of v_{cm} spectrum drops dramatically above 30 MHz with the added RC snubbers, while the amplitude of v_{cm} and i_{cm} spectra below 20 MHz is nearly not affected (see Figure 27c). Apparently, the RC snubbers are very helpful to attenuate EMI at HF range.

7. Conclusions

This paper has investigated EMI in SiC-based motor drives based on modeling and experiment. To quantitatively analyze mechanism of the EMI in motor drive, a simulation model is proposed with sufficient consideration of switching action of the SiC MOSFET and motor impedance, which can be recognized as the key factors on EMI. The effectiveness of the model has been verified through comparisons between model-calculated and experiment-measured results. Then, based on the model, the influence of the motor impedance on EMI has been well investigated with frequency-domain analysis of v_{ds}, v_{phase}, v_{cm}, i_{dm}, i_{cm}. Additionally, impacts of the switching characteristics of SiC MOSFET on EMI have also been discussed in detail with relative experiment results. It can be figured out that:

- The switching behavior of the SiC MOSFET is considered as the source of EMI. With the impacts of the resonances between copper wires, grounding line and parasitic capacitors, the HF harmonics of v_{ds} are changed, which leads to v_{phase} and v_{cm}. Then, with the influence of motor impedance, i_{cm} and i_{dm} can be determined accordingly. As a result, it can be confirmed that the resonances caused by copper wires, grounding line and parasitic capacitors, and motor impedance largely impact the level of EMI below 10 MHz in the motor drive.
- To reduce the spectra spikes in the frequency range above 20 MHz, changing the switching characteristics of the SiC MOSFET is considered as an effective method. With properly selected R_g as well as RC snubber, the HF spectrum peak can be mitigated dramatically. However, in order to reduce the spectra spikes in the frequency range form 1 to 10 MHz, the method described above seems ineffectiveness. The LF (1 to 10 MHz) do not change with the variation of the switching speed and ringing. The spectrum amplitude can be suppressed with the reduced switching frequency at the expense of power density, controllability, and robustness of the motor drive. Thus, in this situation, properly designed EMI filter should be considered to change the CM and DM impedances characteristics around the resonance frequencies (4 and 8 MHz), which can effectively mitigate the spectrum peaks in the LF ranges.

The summaries described above are expected to give much valuable guidance to cope with EMI issues in SiC-based motor drives.

Author Contributions: Y.W. proposed the model, conducted the experiment and composed the manuscript. S.Y., H.L. and M.D. provided valuable comments and suggestions. All authors have read and agreed to the published version of the manuscript

Funding: This work was supported by the National Nature Science Foundation of China (NSFC) under Grant 51807183.

Conflicts of Interest: The authors declare no conflict of interest.

References

1. Wang, F.F.; Zhang, Z. Overview of silicon carbide technology: Device, converter, system, and application. *CPSS Trans. Power Electron. Appl.* **2016**, *1*, 13–32. [CrossRef]
2. Yin, S.; Tseng, K.J.; Simanjorang, R.; Liu, Y.; Pou, J. A 50-kW high-frequency and high-efficiency SiC voltage source inverter for more electric aircraft. *IEEE Trans. Ind. Electron.* **2017**, *64*, 9124–9134. [CrossRef]
3. Lee, W.; Li, S.; Han, D.; Sarlioglu, B.; Minav, T.A.; Pietola, M. A Review of Integrated Motor Drive and Wide-Bandgap Power Electronics for High-Performance Electro-Hydrostatic Actuators. *IEEE Trans. Transp. Electrif.* **2018**, *4*, 684–693. [CrossRef]
4. Sivkov, O.; Novak, M.; Novak, J. Comparison between Si IGBT and SiC MOSFET Inverters for AC Motor Drive. In Proceedings of the 18th International Conference on Mechatronics-Mechatronika (ME), Brno, Czech Republic, 5–7 December 2018; pp. 1–5.
5. Qin, H.; Xie, H.; Zhu, Z.; Nie, X.; Xu, H.; Fu, D. Comparisons of SiC and Si devices for PMSM drives. In Proceedings of the IEEE 8th International Power Electronics and Motion Control Conference (IPEMC-ECCE Asia), Hefei, China, 22–26 May 2016; pp. 891–896.

6. Gong, X.; Ferreira, J.A. Comparison and reduction of conducted EMI in SiC JFET and Si IGBT-based motor drives. *IEEE Trans. Power Electron.* **2014**, *29*, 1757–1767. [CrossRef]
7. Zhang, L.; Yuan, X.; Wu, X.; Shi, C.; Zhang, J.; Zhang, Y. Performance evaluation of high-power SiC MOSFET modules in comparison to Si IGBT modules. *IEEE Trans. Power Electron.* **2019**, *34*, 1181–1196. [CrossRef]
8. Han, D.; Li, S.; Wu, Y.; Choi, W.; Sarlioglu, B. Comparative analysis on conducted CM EMI emission of motor drives: WBG versus Si devices. *IEEE Trans. Ind. Electron.* **2017**, *64*, 8353–8363. [CrossRef]
9. Busse, D.; Erdman, J.; Kerkman, R.J.; Schlegel, D.; Skibinski, G. System electrical parameters and their effects on bearing currents. *IEEE Trans. Ind. Appl.* **1997**, *33*, 577–584. [CrossRef]
10. Magdun, O.; Binder, A. High-frequency induction machine modeling for common mode current and bearing voltage calculation. *IEEE Trans. Ind. Appl.* **2014**, *50*, 1780–1790. [CrossRef]
11. Fan, F.; See, K.Y.; Banda, J.K.; Liu, X.; Gupta, A.K. Simulation of three-phase motor drive system with bearing discharge process. In Proceedings of the Progress in Electromagnetics Research Symposium-Fall (PIERS-FALL), Singapore, 19–22 November 2017; pp. 2091–2097.
12. Moreira, A.F.; Lipo, T.A.; Venkataramanan, G.; Bernet, S. High-frequency modeling for cable and induction motor overvoltage studies in long cable drives. *IEEE Trans. Ind. Appl.* **2002**, *38*, 1297–1306. [CrossRef]
13. Wang, L.; Ho, C.N.M.; Canales, F.; Jatskevich, J. High-frequency modeling of the long-cable-fed induction motor drive system using TLM approach for predicting overvoltage transients. *IEEE Trans. Power Electron.* **2010**, *25*, 2653–2664. [CrossRef]
14. Ran, L.; Gokani, S.; Clare, J.; Bradley, K.J.; Christopoulos, C. Conducted electromagnetic emissions in induction motor drive systems. I. Time domain analysis and identification of dominant modes. *IEEE Trans. Power Electron.* **1998**, *13*, 757–767. [CrossRef]
15. Mirafzal, B.; Skibinski, G.L.; Tallam, R.M.; Schlegel, D.W.; Lukaszewski, R.A. Universal induction motor model with low-to-high frequency-response characteristics. *IEEE Trans. Ind. Appl.* **2007**, *43*, 1233–1246. [CrossRef]
16. Duan, Z.; Zhang, D.; Fan, T.; Wen, X. Prediction of conducted EMI in three phase inverters by simulation method. In Proceedings of the IEEE Transportation Electrification Conference and Expo, Asia-Pacific (ITEC Asia-Pacific), Harbin, China, 7–10 August 2017; pp. 1–6.
17. Zhang, B.; Wang, S. A Survey of EMI Research in Power Electronics Systems with Wide Bandgap Semiconductor Devices. *IEEE J. Emerg. Sel. Top. Power Electron.* **2020**, *8*, 626–643. [CrossRef]
18. Oswald, N.; Anthony, P.; McNeill, N.; Stark, B.H. An experimental investigation of the tradeoff between switching losses and EMI generation with hard-switched all-Si, Si-SiC, and all-SiC device combinations. *IEEE Trans. Power Electron.* **2014**, *29*, 2393–2407. [CrossRef]
19. Fang, Z.; Jiang, D.; Shen, Z.; Qu, R. Impact of application of SiC devices in motor drive on EMI. In Proceedings of the IEEE Applied Power Electronics Conference and Exposition (APEC), Tampa, FL, USA, 26–30 March 2017; pp. 652–658.
20. Moreau, M.; Idir, N.; Le Moigne, P. Modeling of conducted EMI in adjustable speed drives. *IEEE Trans. Electromagn. Compat.* **2009**, *51*, 665–672. [CrossRef]
21. Gong, X.; Ferreira, J.A. Investigation of conducted EMI in SiC JFET inverters using separated heat sinks. *IEEE Trans. Ind. Electron.* **2014**, *61*, 115–125. [CrossRef]
22. Wu, Y.; Bi, C.; Jia, K.; Jin, D.; Li, H.; Yao, W.; Liu, G. High-frequency modelling of permanent magnet synchronous motor with star connection. *IET Electr. Power Appl.* **2018**, *12*, 539–546. [CrossRef]
23. Wu, Y.; Yin, S.; Li, H.; Ma, W. Impact of RC snubber on switching oscillation damping of SiC MOSFET with analytical model. *IEEE J. Emerg. Sel. Top. Power Electron.* **2020**, *8*, 163–178. [CrossRef]
24. Liang, M.; Zheng, T.Q.; Li, Y. An Improved Analytical Model for Predicting the Switching Performance of SiC MOSFETs. *J. Power Electron.* **2016**, *16*, 374–387. [CrossRef]
25. Ahmed, M.R.; Todd, R.; Forsyth, A.J. Predicting SiC MOSFET behavior under hard-switching, soft-Switching, and false turn-on conditions. *IEEE Trans. Ind. Electron.* **2017**, *64*, 9001–9011. [CrossRef]
26. Boglietti, A.; Cavagnino, A.; Lazzari, M. Experimental high-frequency parameter identification of AC electrical motors. *IEEE Trans. Ind. Appl.* **2007**, *43*, 23–29. [CrossRef]

27. Bi, C.; Jia, K.; Wu, Y.; Dong, L.; Li, H.; Yao, W.; Liu, G.; Zhang, H. High-Frequency electric-motor modelling for conducted common-mode current prediction in adjustable speed drive system. *IET Power Electron.* **2018**, *11*, 1257–1265. [CrossRef]
28. Han, D.; Morris, C.T.; Lee, W.; Sarlioglu, B. A case study on common mode electromagnetic interference characteristics of GaN HEMT and Si MOSFET power converters for EV/HEVs. *IEEE Trans. Transp. Electrif.* **2017**, *3*, 168–179. [CrossRef]



© 2020 by the authors. Licensee MDPI, Basel, Switzerland. This article is an open access article distributed under the terms and conditions of the Creative Commons Attribution (CC BY) license (http://creativecommons.org/licenses/by/4.0/).